Supporting Information for

Unprecedented ambient sulphur trioxide (SO_3) detection: possible formation mechanism and atmospheric implications

Lei Yao[1,2#], Xiaolong Fan[1#], Chao Yan[2], Theo Kurtén[3], Kaspar R. Daellenbach[2], Chang Li[1], Yonghong Wang[2], Yishuo Guo[1], Lubna Dada[2], Matti P. Rissanen[4], Jing Cai[2], Yee Jun Tham[2], Qiaozhi Zha[2], Shaojun Zhang[5],Wei Du[2], Miao Yu[6], Feixue Zheng[1], Ying Zhou[1], Jenni Kontkanen[2], Tommy Chan[2], Jiali Shen[2], Joni T Kujansuu[1,2], Juha Kangasluoma[1,2], Jingkun, Jiang[5], Lin Wang[7,8], Douglas R. Worsnop[9], Tuukka Petäjä[2], Veli-Matti Kerminen[2], Yongchun Liu[1], Biwu Chu[2,10,11], Hong He[10,11*], Markku Kulmala[1,2,8*], Federico Bianchi[1,2*]

Affiliations:

[1]Aerosol and Haze Laboratory, Beijing Advanced Innovation Center for Soft Matter Science and Engineering, Beijing University of Chemical Technology, Beijing 100089, China

[2] Institute for Atmospheric and Earth System Research / Physics, Faculty of Science, University of Helsinki, Helsinki 00560, Finland

[3] Department of Chemistry, University of Helsinki, FI-00014 Helsinki 00560, Finland

[4] Aerosol Physics Laboratory, Physics Unit, Tampere University, Tampere 33100, Finland

[5] State Key Joint Laboratory of Environment Simulation and Pollution Control, State Environmental Protection Key Laboratory of Sources and Control of Air Pollution Complex, School of Environment, Tsinghua University, Beijing 100084, China

[6] Institute of Urban Meteorology, China Meteorological Administration, Beijing 100081, China

[7] Shanghai Key Laboratory of Atmospheric Particle Pollution and Prevention (LAP^3), Department of Environmental Science & Engineering, Fudan University, Shanghai 200438, China

[8] Joint International Research Laboratory of Atmospheric and Earth System Sciences (JirLATEST), Nanjing University, Nanjing 210023, China.

[9] Aerodyne Research Inc., Billerica, Massachusetts 01821, USA

[10] State Key Joint Laboratory of Environment Simulation and Pollution Control, Research Center for Eco-Environmental Sciences, Chinese Academy of Sciences, Beijing 100085, China

[11] Center for Excellence in Regional Atmospheric Environment, Institute of Urban Environment, Chinese Academy of Sciences, Xiamen 361021, China

[#] These authors contributed equally.

Corresponding authors:

Markku Kulmala: markku.kulmala@helsinki.fi

Federico Bianchi: federico.bianchi@helsinki.fi

Hong He: honghe@rcees.ac.cn

Text S1. Sampling site

Our field measurements were conducted at BUCT (Beijing University of Chemical Technology) sampling site (39.94° N, 116.30° E), which was located on the west campus of BUCT[1]. This site was located at the roof of a teaching building, which is approximately 15 m above the ground level. Around 130 m to the north and 550 m to the west are Zizhuyuan Road and West Third Ring Road, respectively. The "West Third Ring Road" is one of the main "Ring" roads in Beijing. Besides the influence of traffic, this site is also affected by local commercial and residential activities. Therefore, the BUCT monitoring site is representative of an urban site.

Text S2. The nitrate-CI-APi-LTOF mass spectrometer

A nitrate-based Chemical Ionization - Atmospheric Pressure interface -Long- Time-of-Flight (CI-APi-LTOF, Aerodyne Research Inc, USA and Tofwerk AG, Switzerland) mass spectrometer was deployed to detect SO_3 and gas-phase sulfuric acid. The CI-APi-LTOF consists of an optimized inlet for chemical ionization (CI-inlet)[2, 3] and an APi-LTOF mass spectrometer with the mass resolving power of ~10000 Th/Th. Nitrate ions ($NO_3^-\cdot(HNO_3)_n$, n=0,1 and 2) were used as reagent ions. The working principle of nitrate-CI-APi-LTOF has been described in many previous studies[2, 4].

In the charging part of CI-inlet, the nitrate ions are electrostatically pushed into ambient sample flow to react with SO_3 and H_2SO_4. In the CI-inlet, the ion-molecule reaction time was ~200 ms [4]. Pure air originated from a pure air generator (Aadco 737) was used as the sheath air. Ambient air was sampled into the CI-inlet through a ¾ inch stainless steel tube. A 0.8 L min^{-1} flow from the mixed flow entered the APi-LTOF. Data of CI-APi-LTOF were acquired at 5 s time resolution and analyzed with a MATLAB tofTools package[5].

Text S3. Detection of sulfuric acid with nitrate reagent ions

The ion-molecule reactions of sulfuric acid with nitrate reagent ions can be described by the following reaction[2, 4]:

$$H_2SO_4 + NO_3^-\cdot(HNO_3)_n \rightarrow HSO_4^-\cdot(HNO_3)_j + (n\text{-}j+1)\ HNO_3 \qquad \text{R (S1)}$$

where n = 0, 1 or 2 and j = 0 or 1. Due to H_2SO_4 being a stronger acid, de-protonation occurs during its collision with nitrate ions. Thus, H_2SO_4 molecules can be detected as de-protonated monomer ions and cluster ions with HNO_3 in CI-APi-LTOF.

To take the variation in the total reagent ions into account, neutral sulfuric acid was quantified according to the following equation:

$$[H_2SO_4] = C \times \frac{\sum_{n=0-1}(HSO_4^-).(HNO_3)_n}{\sum_{n=0-2}(NO_3^-)\cdot(HNO_3)_n} \qquad \text{E (1)}$$

where C (in units of cm^{-3}) is a calibration coefficient from in-situ calibration.

Text S4. Calibration experiment for SO_3

The calibration of SO_3 was implemented by introducing a known amount of gaseous SO_3 produced by the reaction of SO_2 and OH radicals formed by UV photolysis of water vapour, which is similar to the method for sulfuric acid calibration in the previous literature (i.e. Kürten et al., 2012) [6]. During the calibration experiment, a 10 L·min^{-1} N_2 flow, a 100 mL·min^{-1} pure air flow, a 300 mL·min^{-1} SO_2 flow and a set of 20 -

400 mL·min^{-1} saturated water vapour flow were mixed together as the calibration sampling flow. Then, the mixed flow was exposed to 184.9 nm UV light to produce OH radicals which reacted with SO_2 to produce SO_3. The schematic of the experimental setup was shown in Figure S2. The UV lamp was turned on in an N_2 environment at least one hour before the actual calibration measurement in order to achieve a stable light intensity. During the calibration, the box was flushed with a 1 - 2 L·min^{-1} dry N_2 flow to avoid the absorption of UV light by O_2. Different levels of SO_3 were achieved by adjusting the flow of saturated water vapour, that is, adjusting OH radical concentrations. The theoretical generated SO_3 concentrations were calculated by Numerical Model which has been introduced in Kürten et al., 2012[6]. The time profiles of water content ($[H_2O]$) and normalized signals of sulfuric acid and SO_3 were exhibited in Figure S3. The correlation between normalized SO_3 signals measured by CI-APi-LTOF and SO_3 concentrations formed by photo-oxidation of SO_2 by OH radicals was depicted in Figure S4. After taking the diffusion loss of the sampling line into account, a calibration coefficient of 1.7×10^{10} molecule cm^{-3} was obtained. The diffusion loss was assumed as same as that of sulfuric acid.

Similar to the quantification of sulfuric acid[2], to regard the variation in the total reagent ions, SO_3 was quantified according to:

$$[SO_3] = C \times \frac{[SO_3 \cdot NO_3^-]}{\sum_{n=0-2}(NO_3^-) \cdot (HNO_3)_n} \qquad \text{E (2)}$$

where C (in units of cm^{-3}) is a calibration coefficient of SO_3.

Text S5. Calculations for collision rate coefficients

Using ion-molecule collision parametrizations from two previous studies (Su & Bowers, 1973 and the Su & Chesnavich, 1982; note that these are the standard approaches used to estimate ion-molecule collision rates also in CIMS studies)[7, 8], with the dipole & polarisability of H_2SO_4 computed at the same level of theory (wB97xd/aug-cc-pVTZ; numerical values given below), the results for the collision rate coefficients (unit cm^3 molecule^{-1} s^{-1}) are as follows:

H_2SO_4 (mass 98)
Dipole moment 3.15093 Debye
Polarisability 35.9657 bohr^3 = 5.330 Ånström^3
Collision rate at 298.15 K with $HNO_3 \cdot NO_3^-$ (mass 125) according to Su & Chesnavich 1982: 2.11E-09
Collision rate at 298.15 K with NO_3^- (mass 62) according to Su & Chesnavich 1982: 2.54E-09
Collision rate at 298.15 K with $HNO_3 \cdot NO_3^-$ (mass 125) according to Su & Bowers 1973: 2.48E-009
Collision rate at 298.15 K with NO_3^- (mass 62) according to Su & Bowers 1973: 2.99E-009

SO_3 (mass 80)
Dipole moment 0 Debye
Polarisability 28.4649 bohr^3 = 4.218 Ånström^3
Collision rate at 298.15 K with $HNO_3 \cdot NO_3^-$ (mass 125) according to Su & Chesnavich 1982: 6.88E-10
Collision rate at 298.15 K with NO_3^- (mass 62) according to Su & Chesnavich 1982: 8.13E-10
Collision rate at 298.15 K with $HNO_3 \cdot NO_3^-$ (mass 125) according to Su & Bowers 1973: 1.79E-009
Collision rate at 298.15 K with NO_3^- (mass 62) according to Su & Bowers 1973: 2.11E-009

The main charging ions are $HNO_3 \cdot NO_3^-$ and NO_3^-. The corresponding ratios (collision rate of H_2SO_4 / collision rate of SO_3) are 3.07, 3.12, 1.39 and 1.42, respectively. The newer ion-molecule collision rate parametrization (Su & Chesnavich, 1982) thus predicts a difference of a factor of 3, whereas the older one only predicts a difference of about a factor of 1.5. A non-polar molecule collides much slower with an ion than a strongly polar molecule. The product ions $H_2SO_4 \cdot NO_3^-$ (binding Gibbs free energy of -32.6 kcal/mol at the wB97xd/aug-cc-pVTZ level) and $SO_3 \cdot NO_3^-$ (binding Gibbs free energy -28.4 kcal/mol at the same level) are very strongly bound and stable. The sensitivity of SO_3 could be less than that of H_2SO_4 by a factor of 3. Thus, a factor of 3 difference would lead to an underestimation of SO_3 if the calibration factor for H_2SO_4 was used to quantify SO_3.

Text S6. Quantum chemical calculations

Quantum chemical calculations demonstrate that the $SO_3 \cdot (NO_3^-)$ cluster is very strongly bound compared to the $HNO_3 \cdot (NO_3^-)$ cluster (Table S1). The difference in binding is over 10 kcal/mol both in electronic and free energies, with the more rigorous coupled-cluster methods predicting a larger difference than the density functional theory method used here. SO_3 molecules will thus be very efficiently charged by nitrate ions in a nitrate-CI-APi-LTOF instrument, as the charge transfer reaction $HNO_3 \cdot (NO_3^-) + SO_3 \rightarrow SO_3 \cdot (NO_3^-) + HNO_3$ is highly favourable. Furthermore, the thermal evaporation rate of $SO_3 \cdot (NO_3^-)$ clusters in the CI-inlet will be negligible, and also the (non-thermal) fragmentation of the cluster in the ion optics of the instrument will be considerably smaller than for example that of the $(H_2SO_4)_2 \cdot HSO_4^-$ cluster, which has binding energy comparable to $HNO_3 \cdot (NO_3^-)$ [9]. All of this supports the hypothesis that the instrument sensitivity toward SO_3 will be very high. The optimized structure of the $SO_3 \cdot (NO_3^-)$ cluster is shown in Figure S5. The strength of the $O_3S \ldots ONO_2^-$ interaction is reflected in the relatively short S…O distance.

The thermodynamics of the $SO_3 \cdot H_2O + NO_3^- \cdot (HNO_3) \rightarrow SO_3 \cdot (NO_3^-) \cdot H_2O + HNO_3$ reaction (R5) was assessed at the wB97X-D/aug-cc-pVTZ level. Three different hydrogen bonding patterns (conformers) for $SO_3 \cdot (NO_3^-) \cdot H_2O$ were assessed, with the H_2O molecule placed either close to the SO_3 moiety, the NO_3^- moiety, or in a bridging position between the two. The latter structure, where H_2O H-bonds to both O-S and O-N oxygen atoms, was found to be the lowest in free energy (at 298 K) (see Figure S6), though the differences between conformers were fairly small (below 2 kcal/mol). By comparison to the results in Table S1, it is likely that higher-level energy corrections (omitted here for computational reasons) would lead to an even more negative (favourable) reaction free energy.

Text S7. Computational details

Molecular and cluster geometries were optimized, and harmonic vibrational frequencies were calculated, with the ωB97X-D density functional [10] and the aug-cc-pVTZ basis set [11], using the Gaussian 16 program suite (Gaussian 16, Revision A.03)[12]. Special care was taken in the optimizations to ensure that SO_3 and NO_3^- had the correct D3h symmetry point group (with a rotational symmetry number of 6). Thermal and vibrational zero-point contributions to enthalpies and entropies were calculated using the standard rigid rotor - harmonic oscillator approximations. Single-point energy corrections were performed on top of the ωB97X-D/aug-cc-pVTZ structures using explicitly correlated coupled cluster theory; specifically RHF-RCCSD(T)-F12[13-15] with the VDZ-F12 and VTZ-F12 basis sets [16]. The Molpro 2015.1 program was used for these calculations (MOLPRO, version 2019.2, a package of ab initio programs, see https://www.molpro.net)[17]. With the smaller basis set, the "F12a" variant was used, based on recommendations in the program manual. With the larger basis set, both "F12a" and "F12b" energies were calculated. The differences between binding energies

computed with the two variants were minimal (around 0.01 kcal/mol or less), and even the difference between the basis sets was less than 0.3 kcal/mol for both $HNO_3 \cdot (NO_3^-)$ and $SO_3 \cdot (NO_3^-)$. Final results are presented using the RHF-RCCSD(T)-F12b/VTZ-F12 values.

Text S8. $PM_{2.5}$, black carbon (BC), particulate sulfate, trace gases, meteorological parameters and UVB measurements.

Mass concentrations of $PM_{2.5}$ were recorded by a TEOM (tapered element oscillating microbalances) monitor. Non-haze and haze days were categorized as daily mean $PM_{2.5}$ mass concentrations of <100 μg m^{-3}, and ≥ 100 μg m^{-3}, respectively.

Mass concentrations of BC in $PM_{2.5}$ were measured by the aethalometer (Magee AE33). $PM_{2.5}$ particles were continuously collected through the filter tape. Then the transmission of light through the filter tape containing the sample was obtained at seven different wavelengths. AE33 calculates the instantaneous concentration of optically absorbing aerosols from the rate of change of the attenuation of light transmitted through the particle-laden filter [18]. The determination of black carbon concentration is based on the measurement of light absorption on a filter loaded. In this study, aerosol particles are continually sampled on the filter, and the optical attenuation is measured with high time resolution 1s. Optical attenuation (ATN) is measured on two spots with different sample flows and the reference spot without the flow calculated as Equation 3:

$$ATN = -100 * \ln\left(\frac{I}{I_0}\right) \qquad \text{E(3)}$$

where I and I_0 represent the detector intensity signal for the measurement spot and reference signal, respectively. The factor 100 is there for convenience only [17].

Airflow (F) is measured after the air passes the filter (Eq.3), lateral airflow in the optical chamber ζ has to be taken into account:

$$F_{in} = F_{out}\,(1 - \zeta) \qquad \text{E(4)}$$

where the value of ζ is determined by measuring input and output flow and was found to be in the 0.02–0.07 range.

Attenuation coefficient (b_{ATN}) and Absorption coefficient (b_{ABS}) can be calculated as Equations 5 and 6

$$b_{ATN} = \frac{S * \left(\frac{\Delta ATN}{100}\right)}{F * \Delta t} \qquad \text{E(5)}$$

$$b_{ABS} = \frac{b_{ATN}}{C} \qquad \text{E(6)}$$

where F is the volumetric flow and S is the filter surface area on which the aerosol particles are deposited, t represents the time, and C is multiple scattering parameter [20].

BC concentration can be calculated using Equation 7:

$$BC = \frac{b_{ABS}}{\sigma_{air}} \qquad \text{E(7)}$$

where σ_{air} is the mass absorption cross-section, here we obtain the mass absorption cross-section value is 7.19 $m^2\,g^{-1}$ measured at 970 nm to convert the observed light attenuation to the mass concentration of BC [21].

Combining Eqs. 5, 6 and 7, we obtain Eq.8 to calculate the concentration of BC:

$$BC = \frac{S * (\frac{\Delta ATN}{100})}{F(1-\zeta) * \sigma_{air} * C * (1 - k * ATN) * \Delta t} \qquad \text{E(8)}$$

where k is a loading effect parameter.

The mass concentrations of non-refractory $PM_{2.5}$ including sulfate concentration were measured by an online Time-of-Flight Aerosol Chemical Speciation Monitor (ToF-ACSM, Aerodyne Research Inc., USA) equipped with a cyclone to select $PM_{2.5}$ particles. Trace gases including SO_2, O_3 and NO_x were recorded by Thermo analyzers (Model 43i, 49i and 42i, Thermo Scientific, USA). A weather station (Vaisala Inc., Finland) was deployed to measure meteorological parameters (ambient relative humidity (RH), temperature, wind speed, visibility). The UVB (280-315 nm) intensity was measured using CUV3 radiometer (Kipp & Zonen, USA). The mixing layer height (MLH) was determined with the enhanced single-lens ceilometers CL-51 (Vaisala Inc., Finland), which utilized the strobe laser lidar technique (910 nm) to measure the attenuated backscattering coefficient profiles. The Vaisala software product BL-VIEW was used to determine the mixing layer height by finding the position with the maximum negative gradient (-dβ/dx) in the attenuated backscattering coefficient profiles as the top of the mixing layer [22].

Text S9. Sub-3 nm particles measurement

The number size distributions of sub-3 nm clusters/particles were measured using an Airmodus A10 particle size magnifier (PSM) coupled with an Airmodus A20 condensation particle counter (CPC) [4, 23]. The measured mobility diameter was from ~1.2 to 2.5 nm. Diethylene glycol and n-butanol were used as working fluids of the PSM and CPC, respectively. The sub-3 nm clusters/particles can grow up to ~90 nm by condensation of diethylene glycol vapour inside the PSM and then detected by the CPC[4]. To minimize the loss of clusters/particles and increase the sampling efficiency, a core sampling system and high flow rate (7.5 L min^{-1}) were utilized [1]. The time resolution of a full scan from 0.1 L min^{-1} to 1.3 L min^{-1} was 240 s.

Text S10. Calculation of condensation sink

Condensation sink (CS) describes the condensing vapour sink caused by the particle population [24]:

$$\mathrm{CS} = 2\pi D \sum_{d_p} \beta_{m,\,d_p} d_p N_{d_p} \qquad E(9)$$

where D is the diffusion coefficient of the condensing vapour (usually assumed to be sulfuric acid), and β_m, dp is the transitional regime correction factor.

Text S11. Source identification of SO_2 in winter

In winter, the median concentrations of SO_2 exhibited similar diurnal trends as SO_3 (Figure 2A). A similar diurnal variation of SO_2 with an early morning peak has already been reported from another site in urban Beijing [25]. We also studied the evaluation of median mixing layer height (MLH) together with the diurnal trend of the median concentration of SO_2, SO_3 and UVB (Figure S8). The median MLH was merely 200-300 m, and stable in the morning (~05:00 to ~08:30). Many studies have reported regional SO_2 is tightly linked with the combustion of sulfur-containing fuels and the smelting of sulfur-containing ores [26-32]. Together with stable weather conditions (Figure S8), the elevated SO_2 concentration during the early morning could mainly be attributed to local emissions (e.g. residential and industry emission) and transportation [33].

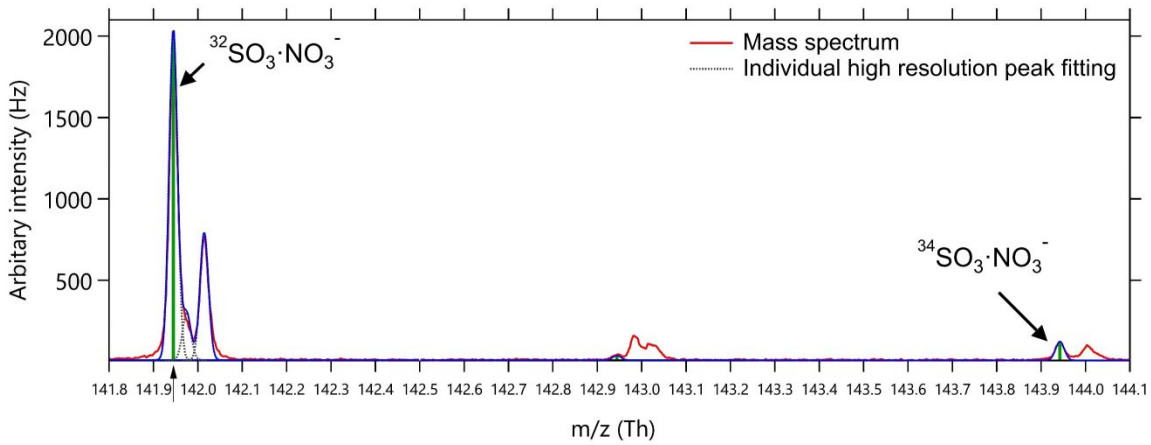

Figure S1. High-resolution peak fitting of the peak $^{32}SO_3 \cdot NO_3^-$ and its main isotope peak $^{34}SO_3 \cdot NO_3^-$.

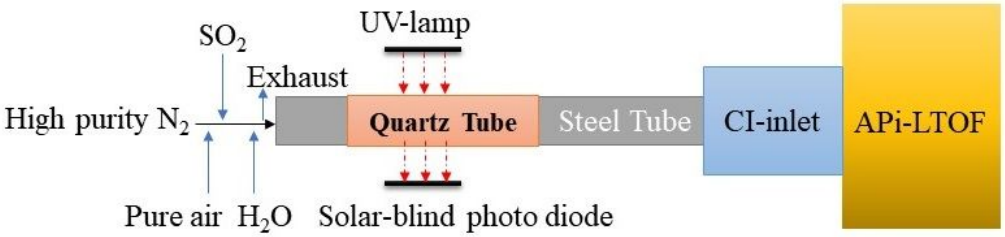

Figure S2. The schematic of the calibration experiment setup.

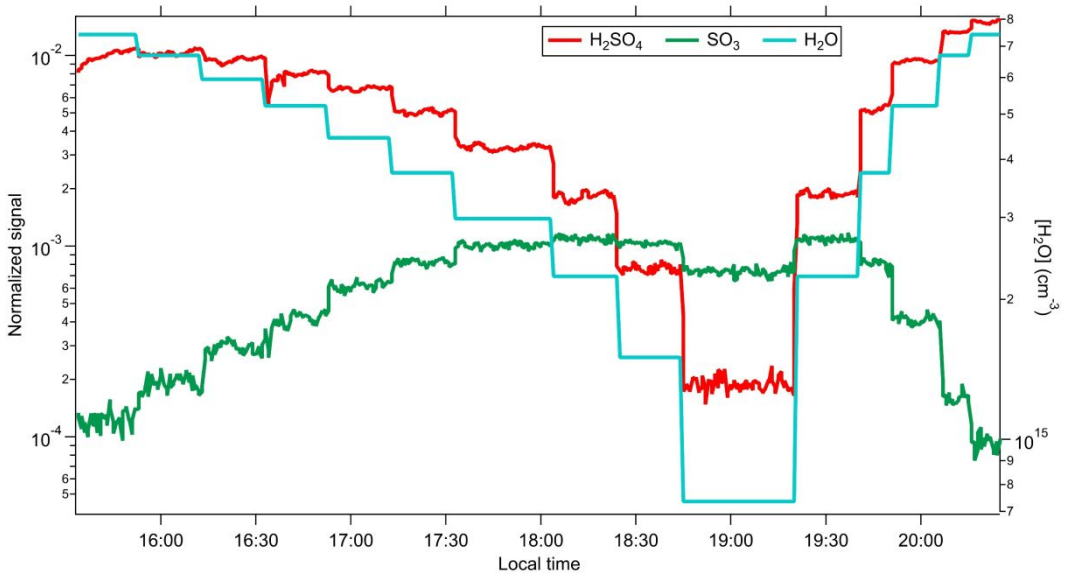

Figure S3. Time series of normalized signals of H_2SO_4 and SO_3, and [H_2O] in the calibration experiment.

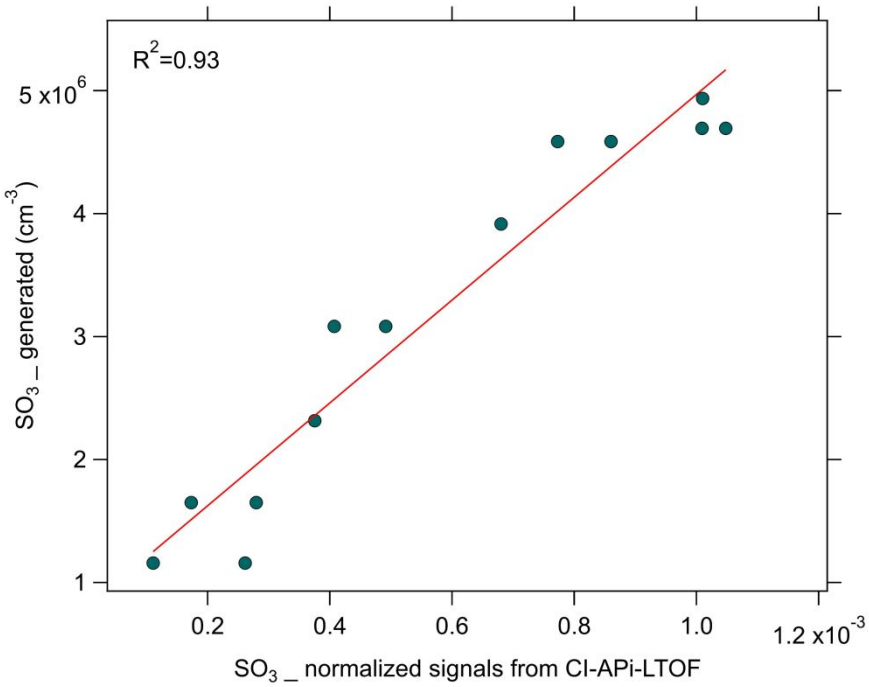

Figure S4. The correlation between normalized SO_3 signals measured by CI-APi-LTOF and SO_3 concentrations formed by the photo-oxidation of SO_2 by OH radicals. Our calibration experiment yielded a calibration coefficient of 1.7×10^{10} cm^{-3} for SO_3. This factor has taken diffusion loss of the sampling line of CI-APi-LTOF into account.

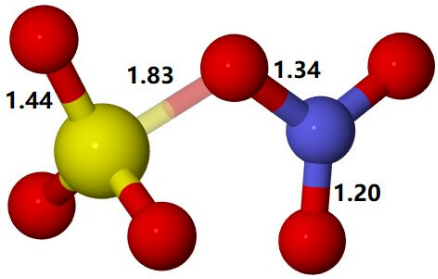

Figure S5. Optimized structure of the $SO_3 \cdot (NO_3^-)$ cluster, at the ωB97X-D/aug-cc-pVTZ level. The S…O interaction between SO_3 and NO_3^- is shown as a covalent bond based on the relatively short interatomic distance, as well as the very strong binding energy. Key bond lengths are given in Ångström. Color coding: yellow=S, blue=N, red=O.

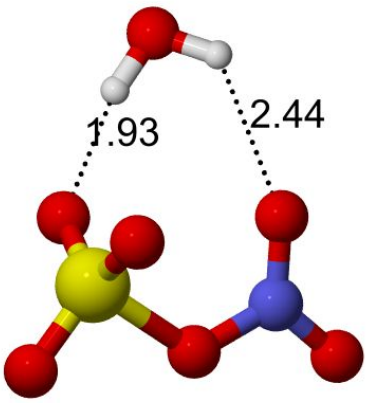

Figure S6. Lowest free energy (at 298 K) structure found for $SO_3 \cdot (NO_3^-) \cdot H_2O$, at the wB97X-D/aug-cc-pVTZ level. Hydrogen bonds are indicated with dotted lines, and the corresponding distances are given in Ångström. Covalent bond lengths differ by less than 0.02 Å from those shown in Figure S5. Color coding: yellow=S, blue=N, red=O.

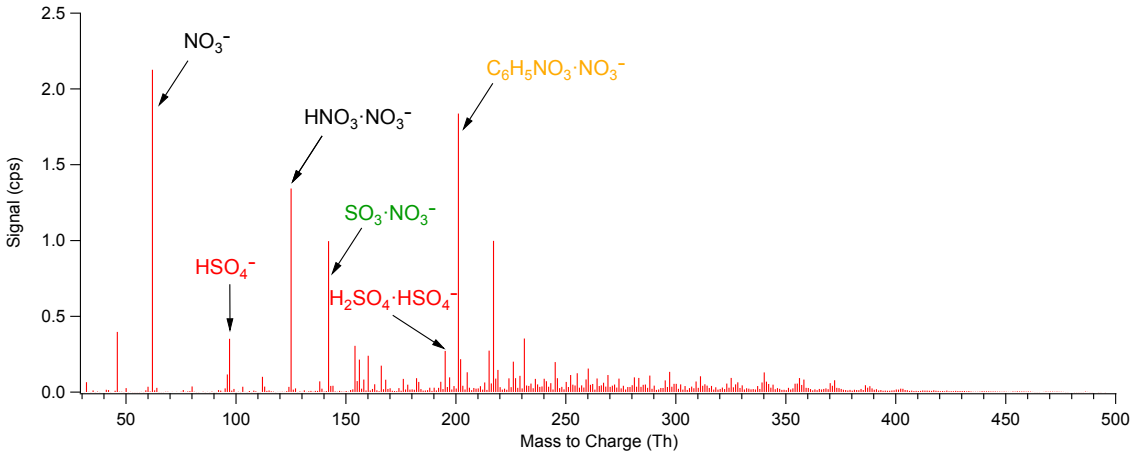

Figure S7. The averaged mass spectra of atmospheric naturally charged ions for one whole day (10 November 2018).

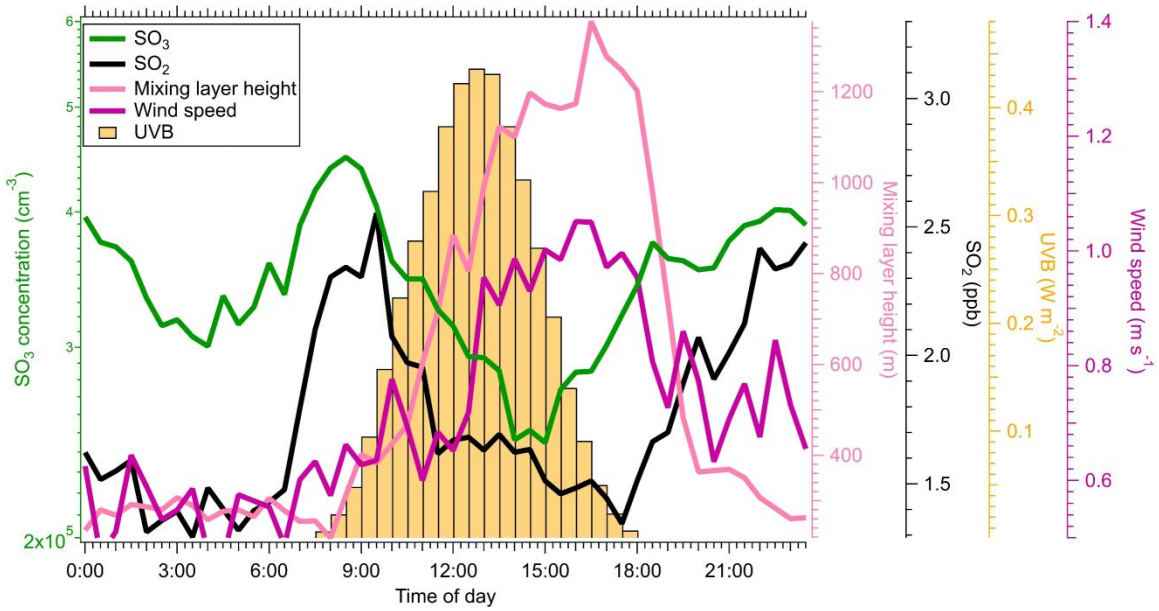

Figure S8. Median diurnal variation of concentrations of SO_3 and SO_2, the mixing layer heights (MLH), intensities of UVB, and wind speeds during winter.

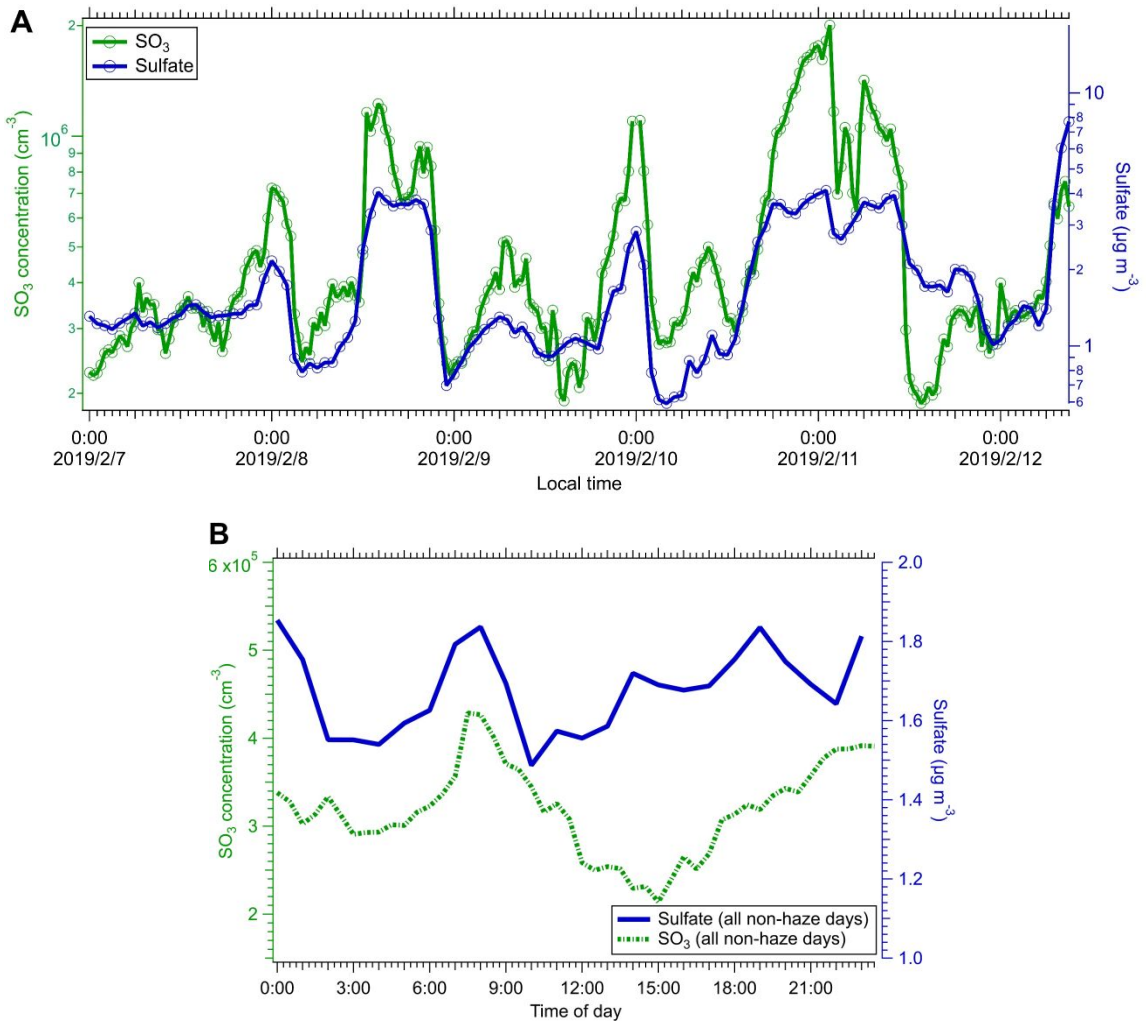

Figure S9. Time profile of SO_3 concentration and mass concentration of sulfate in $PM_{2.5}$ from 7 February to 11 February 2019 (A) and median diel variation of SO_3 and sulfate for all non-haze days during the winter measurement period (B).

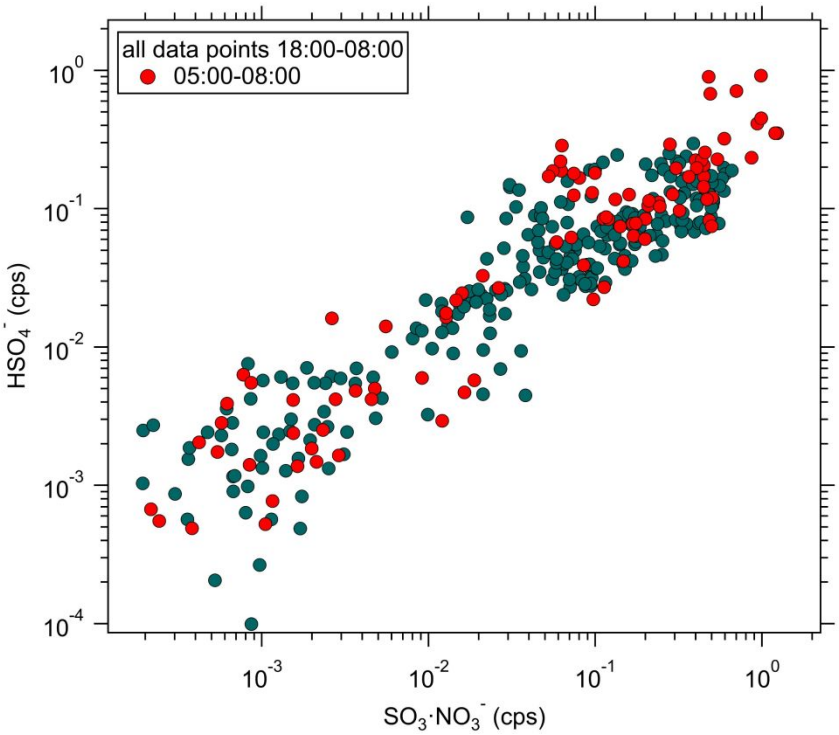

Figure S10. The relationship between the atmospheric ion signals of HSO_4^- and $SO_3 \cdot NO_3^-$ during night time (18:00-5:00 next day) and early morning (5:00-8:00) from 9 to 22 November 2018.

Table S1. Comparison of the binding thermodynamics of $HNO_3 \cdot (NO_3^-)$ and $SO_3 \cdot (NO_3^-)$ ion-molecule clusters, in kcal/mol. ΔE_{DFT} and ΔE_{F12} correspond to the electronic energies (not including vibrational zero-point corrections) computed at the ωB97X-D/aug-cc-pVTZ and RHF-RCCSD(T)-F12b/VTZ-F12 levels, respectively, both at the optimized geometry corresponding to the former method. $\Delta G_{DFT,F12}$ corresponds to the Gibbs free energy (at 298.15 K and 1 atm reference pressure) obtained by combining the RHF-RCCSD(T)-F12b/VTZ-F12 electronic energy with the ωB97X-D/aug-cc-pVTZ thermal and vibrational zero-point contributions.

	ΔE_{DFT}	ΔE_{F12}	$\Delta G_{DFT,F12}$
$HNO_3(NO_3^-)$	-29.1	-29.2	-21.5
$SO_3(NO_3^-)$	-40.1	-44.4	-32.7

References:

1. Zhou, Y.; Dada, L.; Liu, Y.; Fu, Y.; Kangasluoma, J.; Chan, T.; Yan, C.; Chu, B.; Daellenbach, K. R.; Bianchi, F.; Kokkonen, T. V.; Liu, Y.; Kujansuu, J.; Kerminen, V.-M.; Petäjä, T.; Wang, L.; Jiang, J.; Kulmala, M., Variation of size-segregated particle number concentrations in wintertime Beijing. *Atmos. Chem. Phys.* **2020,** *20*, (2), 1201-1216.

2. Jokinen, T.; Sipilä, M.; Junninen, H.; Ehn, M.; Lönn, G.; Hakala, J.; Petäjä, T.; Mauldin, R. L.; Kulmala, M.; Worsnop, D. R., Atmospheric sulphuric acid and neutral cluster measurements using CI-APi-TOF. *Atmos. Chem. Phys.* **2012,** *12*, (9), 4117-4125.

3. Eisele, F. L.; Tanner, D. J., Measurement of the Gas-Phase Concentration of H_2SO_4 and Methane Sulfonic-Acid and Estimates of H_2SO_4 Production and Loss in the Atmosphere. *J. Geophys. Res-Atmos.* **1993,** *98*, (D5), 9001-9010.

4. Yao, L.; Garmash, O.; Bianchi, F.; Zheng, J.; Yan, C.; Kontkanen, J.; Junninen, H.; Mazon, S. B.; Ehn, M.; Paasonen, P.; Sipila, M.; Wang, M.; Wang, X.; Xiao, S.; Chen, H.; Lu, Y.; Zhang, B.; Wang, D.; Fu, Q.; Geng, F.; Li, L.; Wang, H.; Qiao, L.; Yang, X.; Chen, J.; Kerminen, V. M.; Petaja, T.; Worsnop, D. R.; Kulmala, M.; Wang, L., Atmospheric new particle formation from sulfuric acid and amines in a Chinese megacity. *Science* **2018,** *361*, (6399), 278-281.

5. Junninen, H.; Ehn, M.; Petaja, T.; Luosujarvi, L.; Kotiaho, T.; Kostiainen, R.; Rohner, U.; Gonin, M.; Fuhrer, K.; Kulmala, M.; Worsnop, D. R., A high-resolution mass spectrometer to measure atmospheric ion composition. *Atmos. Meas. Tech.* **2010,** *3*, (4), 1039-1053.

6. Kurten, A.; Rondo, L.; Ehrhart, S.; Curtius, J., Calibration of a chemical ionization mass spectrometer for the measurement of gaseous sulfuric acid. *J. Phys. Chem. A* **2012,** *116*, (24), 6375-86.

7. Su, T.; Bowers, M. T., Ion-Polar Molecule Collisions - Effect of Molecular-Size on Ion-Polar Molecule Rate Constants. *J. Am. Chem. Soc.* **1973,** *95*, (23), 7609-7610.

8. Su, T.; Chesnavich, W. J., Parametrization of the Ion-Polar Molecule Collision Rate-Constant by Trajectory Calculations. *J. Chem. Phys.* **1982,** *76*, (10), 5183-5185.

9. Passananti, M.; Zapadinsky, E.; Zanca, T.; Kangasluoma, J.; Myllys, N.; Rissanen, M. P.; Kurten, T.; Ehn, M.; Attoui, M.; Vehkamaki, H., How well can we predict cluster fragmentation inside a mass spectrometer? *Chem. Commun.* **2019,** *55*, (42), 5946-5949.

10. Chai, J. D.; Head-Gordon, M., Long-range corrected hybrid density functionals with damped atom-atom dispersion corrections. *Phys. Chem. Chem. Phys.* **2008,** *10*, (44), 6615-6620.

11. Woon, D. E.; Dunning, T. H., Gaussian-Basis Sets for Use in Correlated Molecular Calculations .III. The Atoms Aluminum through Argon. *J. Chem. Phys.* **1993,** *98*, (2), 1358-1371.

12. Gaussian 16, Revision A.03, Frisch, M. J.; Trucks, G. W.; Schlegel, H. B.; Scuseria, G. E.; Robb, M. A.; Cheeseman, J. R.; Scalmani, G.; Barone, V.; Petersson, G. A.; Nakatsuji, H.; Li, X.; Caricato, M.; Marenich, A. V.; Bloino, J.; Janesko, B. G.; Gomperts, R.; Mennucci, B.; Hratchian, H. P.; Ortiz, J. V.; Izmaylov, A. F.; Sonnenberg, J. L.; Williams-Young, D.; Ding, F.; Lipparini, F.; Egidi, F.; Goings, J.; Peng, B.; Petrone, A.; Henderson, T.; Ranasinghe, D.; Zakrzewski, V. G.; Gao, J.; Rega, N.; Zheng, G.; Liang, W.; Hada, M.; Ehara, M.; Toyota, K.; Fukuda, R.; Hasegawa, J.; Ishida, M.; Nakajima, T.; Honda, Y.; Kitao, O.; Nakai, H.; Vreven, T.; Throssell, K.; Montgomery, J. A., Jr.; Peralta, J. E.; Ogliaro, F.; Bearpark, M. J.; Heyd, J. J.; Brothers, E. N.; Kudin, K. N.; Staroverov, V. N.; Keith, T. A.; Kobayashi, R.; Normand, J.; Raghavachari, K.; Rendell, A. P.; Burant, J. C.; Iyengar, S. S.; Tomasi, J.; Cossi, M.; Millam, J. M.; Klene, M.; Adamo, C.; Cammi, R.; Ochterski, J. W.; Martin, R. L.; Morokuma, K.; Farkas, O.; Foresman, J. B.; Fox, D. J. Gaussian, Inc., Wallingford CT, **2016**.

13. Adler, T. B.; Knizia, G.; Werner, H. J., A simple and efficient CCSD(T)-F12 approximation. *J. Chem. Phys.* **2007,** *127*, (22).

14. Knizia, G.; Adler, T. B.; Werner, H. J., Simplified CCSD(T)-F12 methods: Theory and benchmarks. *J. Chem. Phys.* **2009,** *130*, (5).

15. Werner, H. J.; Knizia, G.; Manby, F. R., Explicitly correlated coupled cluster methods with pair-specific geminals. *Mol. Phys.* **2011,** *109*, (3), 407-417.

16. Peterson, K. A.; Adler, T. B.; Werner, H. J., Systematically convergent basis sets for explicitly correlated wavefunctions: The atoms H, He, B-Ne, and Al-Ar. *J. Chem. Phys.* **2008,** *128*, (8).

17. MOLPRO, version 2019.2, a package of ab initio programs, Werner, H.-J.; Knowles, P. J.; Knizia,G.; Manby, F. R.; Schütz, M.; Celani, P.; Györffy, W.; Kats, D.; Korona, T.; Lindh, R.; Mitrushenkov, A.; Rauhut, G.; Shamasundar, K. R.; Adler, T. B.; Amos, R. D.; Bennie, S. J.; Bernhardsson, A.; Berning, A.; Cooper, D. L.; Deegan, M. J. O.; Dobbyn, A. J.; Eckert, F.; Goll, E.; Hampel, C.; Hesselmann, A.; Hetzer, G.; Hrenar, T.; Jansen, G.; Köppl, C.; Lee, S. J. R.; Liu, Y.; Lloyd, A. W.; Ma, Q.; Mata, R. A.; May, A. J.; McNicholas, S. J.; Meyer, W.; Miller III, T. F.; Mura, M. E.; Nicklass, A.; O'Neill, D. P.; Palmieri, P.; Peng, D.; Pflüger, K.; Pitzer, R.; Reiher, M.; Shiozaki, T.; Stoll, H.; Stone, A. J.; Tarroni, R.; Thorsteinsson, T.; Wang, M.; and Welborn, M. see https://www.molpro.net.

18. Drinovec, L.; Močnik, G.; Zotter, P.; Prévôt, A. S. H.; Ruckstuhl, C.; Coz, E.; Rupakheti, M.; Sciare, J.; Müller, T.; Wiedensohler, A., The "dual-spot" Aethalometer: an improved measurement of aerosol black carbon with real-time loading compensation. *Atmos. Meas. Tech.* **2014,** *8*, (5), 1965-1979.

19. Gundel, L. A.; Dod, R. L.; Rosen, H.; Novakov, T., The Relationship between Optical Attenuation and Black Carbon Concentration for Ambient and Source Particles. *Sci. Total Environ.* **1984,** *36*, (Jun), 197-202.

20. Weingartner, E., Saathoff, H., Schnaiter, M., Streit, N., Bitnar, B., and Baltensperger, U., Absorption of light by soot particles: determination of the absorption coefficient by means of aethalometers. *J. Aerosol Sci*. **2003**.*34*, 1445 – 1463.

21. Zotter, P.; Herich, H.; Gysel, M.; El-Haddad, I.; Zhang, Y.; Močnik, G.; Hüglin, C.; Baltensperger, U.; Szidat, S.; Prévôt, A. S. H., Evaluation of the absorption Ångström exponents for traffic and wood burning in the Aethalometer-based source apportionment using radiocarbon measurements of ambient aerosol. *Atmos. Chem. Phys.* **2017,** *17*, (6), 4229-4249.

22. Munkel, C.; Eresmaa, N.; Rasanen, J.; Karppinen, A., Retrieval of mixing height and dust concentration with lidar ceilometer. *Bound-Lay Meteorol* **2007,** *124*, (1), 117-128.

23. Vanhanen, J.; Mikkila, J.; Lehtipalo, K.; Sipila, M.; Manninen, H. E.; Siivola, E.; Petaja, T.; Kulmala, M., Particle Size Magnifier for Nano-CN Detection. *Aerosol Sci. Technol.* **2011,** *45*, (4), 533-542.

24. Kulmala, M.; Petaja, T.; Nieminen, T.; Sipila, M.; Manninen, H. E.; Lehtipalo, K.; Dal Maso, M.; Aalto, P. P.; Junninen, H.; Paasonen, P.; Riipinen, I.; Lehtinen, K. E. J.; Laaksonen, A.; Kerminen, V. M., Measurement of the nucleation of atmospheric aerosol particles. *Nat. Protoc.* **2012,** *7*, (9), 1651-1667.

25. Xu, W. Y.; Zhao, C. S.; Ran, L.; Lin, W. L.; Yan, P.; Xu, X. B., SO_2 noontime-peak phenomenon in the North China Plain. *Atmos. Chem. Phys.* **2014,** *14*, (15), 7757-7768.

26. Li, R.; Fu, H. B.; Cui, L. L.; Li, J. L.; Wu, Y.; Meng, Y.; Wang, Y. T.; Chen, J. M., The spatiotemporal variation and key factors of SO_2 in 336 cities across China. *J. Clean. Prod.* **2019,** *210*, 602-611.

27. Huang, Q.; Cheng, S. Y.; Perozzi, R. E.; Perozzi, E. F., Use of a MM5-CAMx-PSAT Modeling System to Study SO_2 Source Apportionment in the Beijing Metropolitan Region. *Environ. Model. Assess.* **2012,** *17*, (5), 527-538.

28. Kampa, M.; Castanas, E., Human health effects of air pollution. *Environ. Pollut.* **2008,** *151*, (2), 362-367.

29. Zhong, Q. R.; Shen, H. Z.; Yun, X.; Chen, Y. L.; Ren, Y. A.; Xu, H. R.; Shen, G. F.; Ma, J. M.; Tao, S., Effects of International Fuel Trade on Global Sulfur Dioxide Emissions. *Environ. Sci. Tech. Let.* **2019,** *6*, (12), 727-731.

30. Klimont, Z.; Smith, S. J.; Cofala, J., The last decade of global anthropogenic sulfur dioxide: 2000-2011 emissions. *Environ. Res. Lett.* **2013,** *8*, (1).

31. Su, S. S.; Li, B. G.; Cui, S. Y.; Tao, S., Sulfur Dioxide Emissions from Combustion in China: From 1990 to 2007. *Environ. Sci. Technol.* **2011,** *45*, (19), 8403-8410.

32. Zheng, H. T.; Cai, S. Y.; Wang, S. X.; Zhao, B.; Chang, X.; Hao, J. M., Development of a unit-based industrial emission inventory in the Beijing-Tianjin-Hebei region and resulting improvement in air quality modeling. *Atmos. Chem. Phys.* **2019,** *19*, (6), 3447-3462.

33. Liu, J.; Mauzerall, D. L.; Chen, Q.; Zhang, Q.; Song, Y.; Peng, W.; Klimont, Z.; Qiu, X. H.; Zhang, S. Q.; Hu, M.; Lin, W. L.; Smith, K. R.; Zhu, T., Air pollutant emissions from Chinese households: A major and underappreciated ambient pollution source. *Proc. Natl. Acad. Sci. U.S.A.* **2016,** *113*, (28), 7756-7761.